atmosphere

MDPI

Article

Regional Evolution of the Meteosat Solar and Infrared Spectra (2005–2024) Linked to Cloud Cover and Ocean Surface

José I. Prieto-Fernández [1] and Humberto A. Barbosa [2,*]

[1] PraproSL, 06420 Castuera, Spain; jprieto@prapro.com
[2] Satellite Image Processing and Analysis Laboratory (LAPIS), Federal University of Alagoas (UFAL), A C Simões Campus, Maceió 57072-900, Brazil
* Correspondence: humberto.barbosa@icat.ufal.br; Tel.: +55-8-299-999-3043

Abstract

We analyze the evolution of atmospheric and surface physical properties over the region of the Earth observed by the Meteosat Second Generation (MSG) satellites during the period 2005–2024. Long-term changes are detected in the observed radiances, with a decrease in the solar domain (−1.3%) and an increase in the thermal infrared domain (+0.4%), consistent with trends reported by independent broadband radiometers such as CERES. The outgoing solar radiance (OSR) exhibits a marked decline, which we associate with a reduction in low-level cloud cover within the nominal Meteosat field of view (MFoV) centered at 0° longitude. Changes in atmospheric CO_2 concentration also contribute to the observed radiative imbalance at the top of the atmosphere (TOA). Instrument calibration stability and inter-satellite homogenization across the MSG series are explicitly addressed, enabling the detection of robust interdecadal signals. By subdividing the MFoV into 60 regional sectors, we characterize spatial variations in cloud amount at low and high atmospheric levels and relate these changes to regional TOA radiative imbalances and concurrent variations in Atlantic sea surface temperature (SSTs). The spectral information provided by SEVIRI allows a more detailed attribution of radiative changes than broadband observations alone from other instruments. In particular, radiances measured in the atmospheric split-window region near 11 μm are shown to be sensitive to variations in low-tropospheric humidity, which exhibits a widespread decadal-scale increase. The results indicate a close coupling between cloud-cover changes, radiative fluxes, and SST evolution on the recent interdecadal time scale. The observed decrease in low-level total cloud cover is independently in line with ECMWF ERA5 reanalysis data. These findings highlight the value of long, stable geostationary observations for investigating atmosphere–ocean interactions and their role in regional climate variability.

Keywords: satellite observations; radiance; absorption of thermal radiation; radiation flux; long-term series

Academic Editor: Doris Folini

Received: 27 February 2026
Revised: 7 April 2026
Accepted: 8 April 2026
Published: 10 April 2026

1. Introduction

Meteorological satellites provide continuous observations of the spectral radiance reflected and emitted by the Earth–atmosphere system. These measurements are sensitive to key physical variables, including cloud cover, atmospheric temperature and humidity, and the concentration of radiatively active gases and aerosols. Together, these variables regulate the Earth's radiative balance and exert a primary control on surface temperature [1].

Perturbations to the radiative balance, arising from both natural climate variability and anthropogenic forcing, manifest as surface warming with a pronounced regional structure. Satellite observations from low-Earth orbit [2] and geostationary platforms [3,4] are routinely used to derive components of the Earth's Radiation Budget (ERB) at the top of the atmosphere (TOA), which is recognized as an Essential Climate Variable [5]. The Meteosat Second Generation (MSG) geostationary satellite series has provided continuous measurements since 2004, with a temporal sampling of 15 min, enabling the characterization of diurnal to interdecadal variations in TOA radiative fluxes [6–8].

The use of MSG data for climate-scale analyses requires a careful assessment of instrument calibration stability and inter-satellite consistency. SEVIRI radiances have been inter-calibrated against the MODIS instrument aboard the Aqua satellite using collocated near-nadir observations, accounting for differences in spectral response functions [9]. Previous studies have demonstrated that the operational SEVIRI calibration is stable and robust across a range of viewing and illumination geometries, with brightness temperature differences typically in the order of 0.1 K for most thermal infrared channels, and larger deviations confined primarily to the CO_2 absorption band near 13.4 μm, which is intermittently affected by ice contamination [10]. Hewison outlines the methods employed to achieve data homogeneity across the Meteosat series, incorporating multiple satellites and sensors, including corrections for sensor degradation [10]. The consistency of MSG-based trends with independent estimates from CERES and ERA5 provides an additional basis for assessing the robustness of the derived radiative signals [11].

Recent reviews have emphasized the value of spectrally resolved satellite radiance measurements for evaluating climate variability and for constraining climate model behavior beyond what is accessible from broadband fluxes alone [12]. In this context, the long-term evolution of outgoing longwave radiation (OLR) inferred from Meteosat observations merits particular attention. While surface warming is expected to lead to increased thermal emission according to the Stefan–Boltzmann relationship, the aggregate non-solar SEVIRI radiances exhibit only a weak positive trend over the study period. This behavior suggests that compensating processes, including cloud and water-vapor changes, play a significant role in modulating the ToA radiative response, and that changes in the reflected solar component may contribute substantially to the observed increasing imbalance between incoming solar radiation and energy re-emitted to space [13].

Building on previous work by the authors [14], the present study investigates the regional structure of TOA radiative imbalance and its relationship with sea surface temperature (SST) variability in the Atlantic and western Indian Oceans, using SEVIRI radiance measurements acquired between 2005 and 2024. By subdividing the Meteosat field of view into multiple regional sectors, we examine spatial variations in low- and high-level cloud cover and assess their contribution to observed radiative trends.

Cloud feedback remains one of the largest sources of uncertainty in climate projections. As noted in the IPCC Fifth Assessment Report (AR5), low clouds tend to contribute positive feedback in most climate models, yet the underlying mechanisms and their representation remain incompletely understood [15,16]. Although satellite observations face inherent challenges in separating cloud layers, the high temporal sampling and long-term consistency of geostationary measurements allow for a regionally resolved analysis that can help elucidate the role of low-level cloud variability in recent climate trends. The results presented here provide observational constraints on cloud–radiation–SST coupling derived exclusively from satellite measurements.

2. Data and Methods

The method used in this study is described in a previous work [14], and is here upgraded and applied to a longer time period. The use of a longer data series is more representative of the recent climate, and has reduced the uncertainty of the results by 45% as a consequence of a wider database (from 12 to 20 years) and 4 × 4 pixel grouping. Each complete set of measurements of the whole Meteosat Field of View (MFoV) on an operational cycle of 15 min is considered a 'slot'. We compare slot and channel average radiances for an initial period of time ('ancient', from January 2005 to December 2014) with radiances for a final period ('recent', from January 2015 to December 2024), to determine data trends over ten years (See Table 1).

The SEVIRI radiometer (EUMETSAT, Darmstadt, Germany) on board MSG scans the MFOV at eleven different wavelengths, with sub-satellite point horizontal resolution of 3 km × 3 km. The achieved data resolution is better than ±0.1 K for brightness temperatures, as a result of data grouping in 4 × 4 pixel boxes.

Data differences are built with a lag of 522 weeks, approximately ten years. For example, we compare the MFOV average data in the Meteosat slot at the nominal date and time Friday 7 January 2005 at 12 00 UTC with the slot on Friday 9 January 2015 at 12 00 UTC, and so on for subsequent pairs of slots. Based on all pairs separated by approximately ten years, we build a good estimate of the change in slot-averaged radiances in the eleven Meteosat SEVIRI channels (see Table 2). We choose a constant weekday for all the slot comparisons to avoid possible minor changes in the images due to different human activities on different weekdays. This weekly choice, rather than a more frequent data sampling, proves robust, since a week is a typical decoupling time for satellite images, as far as the autocorrelation function is concerned (Pearson correlation ~0.48). Pearson coefficients in this paper are calculated on the original trend in the series.

We define the terms radiance and flux in this paper as follows. Radiance is measured in units $mW{\cdot}m^{-2}{\cdot}sr^{-1}{\cdot}(cm^{-1})^{-1}$, where mW stands for milliwatt, m for meter and sr for steradian, the solid angle unit. We refer to that radiance unit in the figures as SRU, the standard radiance unit. Radiance is the power per surface unit, per steradian and per wavenumber unit. Flux (in $W{\cdot}m^{-2}$ units), also named integrated radiance or irradiance, is the result of integrating in the spectral domain, and in solid angle (by using the factor π), the radiance measured by the satellite.

As an example, Figure 1 shows the slot-averaged radiance around 0.6 μm measured by Meteosat. Radiance values oscillate between 3.2 SRU around June–July, the least cloudy period in the year, and 4.6 SRU around the equinoxes. Dots with the differences in ten years (Figure 1a) form a cluster biased to a negative value around −0.1 SRU, indicating a decrease in reflected radiation, plausibly corresponding to a significant decrease in cloud cover for all seasons. In the scatter plot in Figure 1a, the months of June and July present the lowest average reflectivity in the year. Cloud loss in a decade is, however, similar for all times in the year. The scatter plot in Figure 1b relates average reflectivity to the contrast (standard deviation) in the satellite image, higher in the presence of abundant cloud, as is the case around equinoxes.

The time series (in Figure 1c,d, before and after de-seasonalizing) shows a clear statistical trend (Mann–Kendall, $Z = -5.00$, $p < 0.001$), and all values in Figure 1d in the decade 2015–2024 for 0.6 μm radiances are below those ten years before. This result coincides with the results for CERES [11].

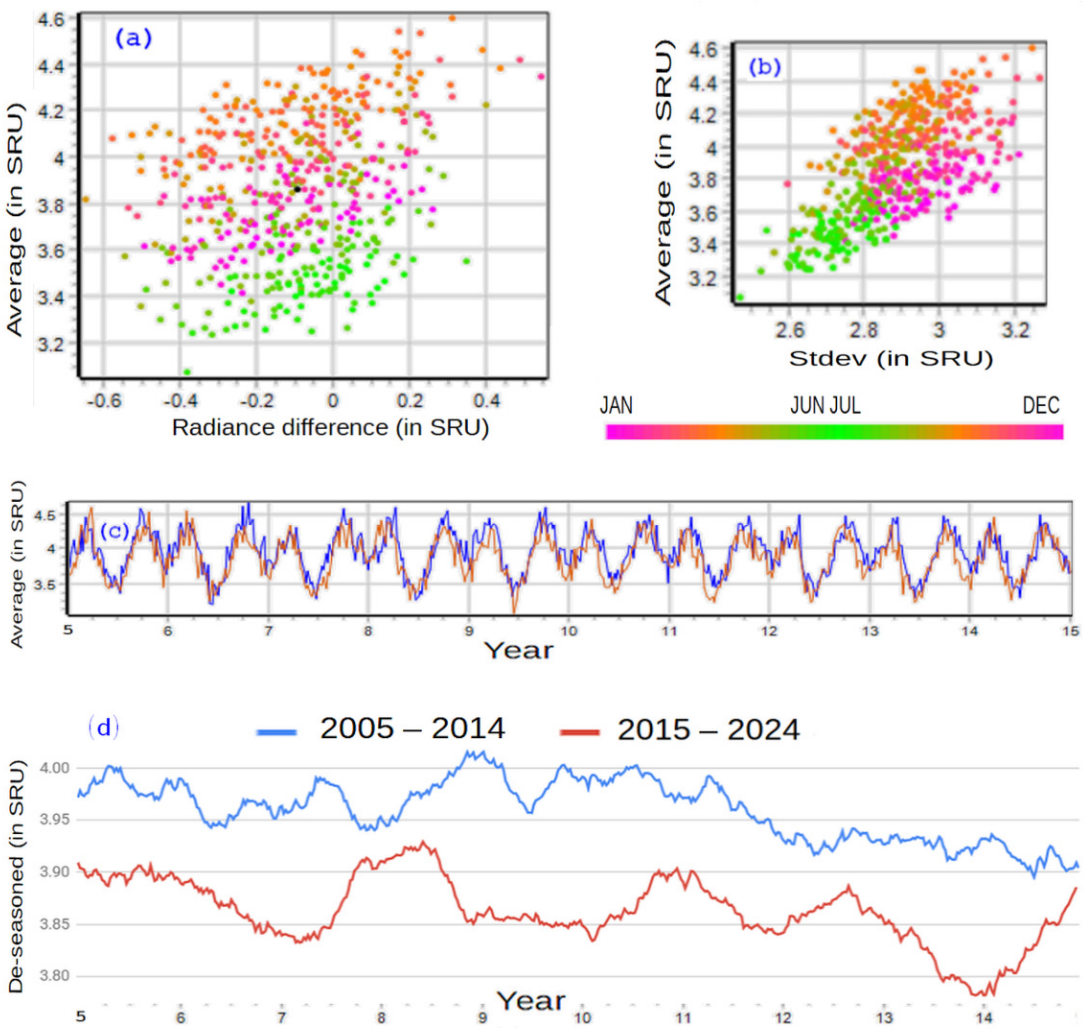

Figure 1. Evolution of average radiance values measured on Meteosat channel 0.6 μm, in SRU units, explained in the main text. (**a**) Scatter plot of differences in the slot averages (horizontal axis) for slots separated by precisely 10 years ±2 days, compared with the 'recent' slot average (vertical axis) of that difference, showing a significant radiance reduction in a decade (black dot is the distribution center of mass). (**b**) Scatter plot for the connection between 'recent' slot average values (vertical) and standard deviation inside the slot (horizontal, a measure of pixel radiance uniformity and a proxy for cloud amount in the scene). Dot colors for (**a**,**b**) indicate month of the year, with highest values showing around the equinoxes. (**c**) Comparison of reflected radiance values at 0.6 μm for a time lapse of ten years: brown line for 'recent' and blue line for 'ancient' radiance, with the 'recent' typically higher in value. The yearly cycle of radiance shows two high peaks around the equinoxes in the MFoV. (**d**) The same as in (**c**), after deseasonalizing the series, to mark the most critical moments in the evolution of solar radiance around 0.6 μm.

For confirmation that this is not linked to calibration artifacts, we found in the ERA-5 database of atmospheric reanalysis a parallel evolution of the total cloud cover ('TCC') averaged for the area between geographical latitudes = (−50°, 50°) and longitudes = (−70°, 70°), with a Pearson correlation before detrending between the two series of 0.71, which indicates a reassuring agreement with an external reference (Figure 2). Recent trend discrepancies remain unexplained, but will hopefully be clarified when fresh data from 2025 and 2026 are added to the study.

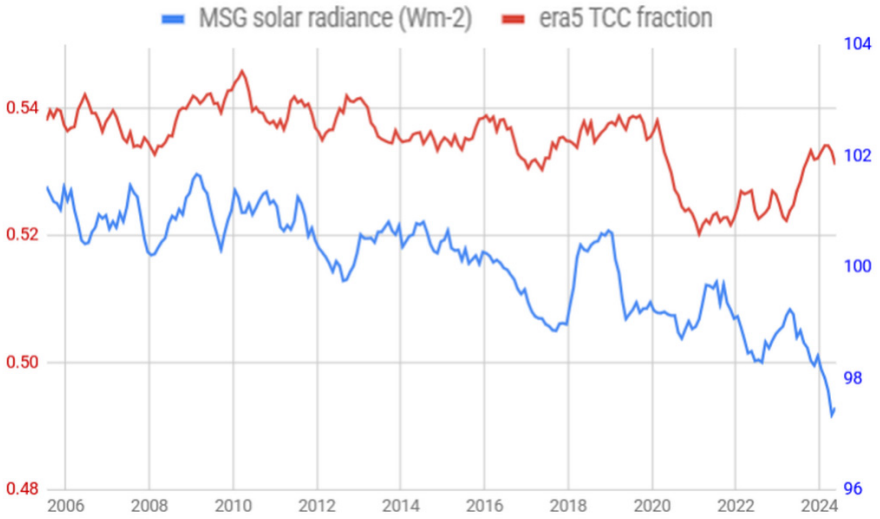

Figure 2. Temporal comparison of integrated solar reflected radiances in the MFoV, and the ERA-5 total cloud cover for the area latitude = (−50°, 50°) and longitude = (−70°, 70°). The series were de-seasonalized. Expected discrepancies due to cloud type and phase do not blur the time downward trend in both magnitudes, with a Pearson correlation of 0.71. Radiances (in blue) are expressed in Wm^{-2}. Their time series allows a direct comparison with the total cloud-cover fraction from ERA-5.

A 24 h period between images shows typical Pearson correlation coefficients of 0.95 ± 0.02, but only 0.48 ± 0.05 if the two images are separated by one week. If we compare monthly image averages for consecutive months, where the rapid movement of cloud is averaged out, the correlation grows to 0.71 ± 0.03. Longer period averages increase the correlation, i.e., an averaged year is very similar to the next averaged year. And for longer averages, the 0.6 μm solar correlation between 10-year averages of 0.6 μm solar images reaches 0.994.

Table 1. Data set composition (European date format).

Meteosat Dataset	Points	Periodicity	Start Date	End Date
ancient	522	weekly	31 December 2004	26 December 2014
recent	522	weekly	2 January 2015	27 December 2024

On an initial (ancient) and a final (recent) period, each one ten years long (3647 days or 521 weeks) consisting of 522 slots, we attain statistical significance for most channels.

We use the 522 pairs of slots for three kinds of statistical analyses: (a) MFoV pixel average for each channel used to estimate trends, in Figure 3. (b) Local change in pixel averages for all pixels, shown in Figure 4, for two of the channels. (c) Pixel sampling for inter-channel comparisons in Figure 5.

The characteristics of the SEVIRI channels are shown in the first four columns of Table 2. The information from Meteosat is available at the EUMETSAT data portal https://user.eumetsat.int (free registration is required to access data). We extracted calibrated and rectified (level 1.5) radiances from December 2004 to December 2024 at 12 UTC in the MFOV from the satellite at 0° longitude. Data are retrieved as files with a count value for each pixel, channel and nominal time. The count value is converted into spectral radiance units (SRUs) with the help of the slot calibration coefficients in each retrieved file. In this study, we restrict ourselves to the slot labeled 12 UTC, which contains MFOV data captured between 1200 UTC and 1212 UTC, acquired from south to north, roughly corresponding to midday conditions at the Greenwich meridian. The trends estimated in this study (defined here as the change between the final and initial measurements) are

the differences in slot-average values measured with a 10-year interval on the 11 different channels of SEVIRI (see Table 2).

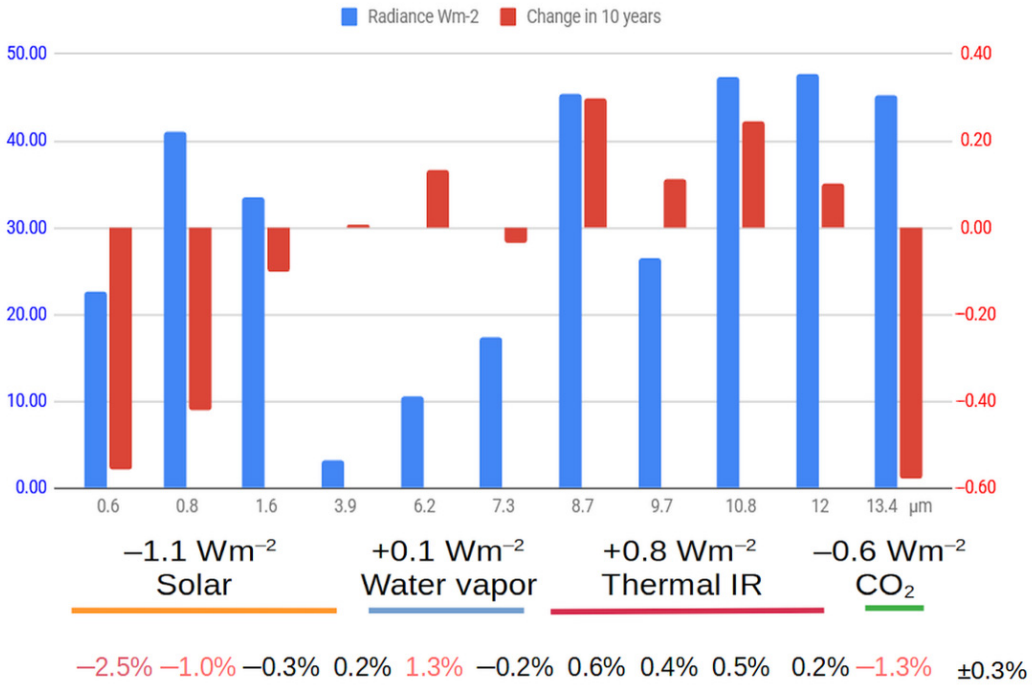

Figure 3. Decadal radiance average (in blue) and change (in red) in the period 2005 to 2024 for the eleven MSG channels on the horizontal axis, as defined in Table 2, in Wm^{-2}. Blue bars indicate the integrated radiance around the central wavelength. Red bars show the decadal change. The x-axis shows the central wavelength of 11 SEVIRI channels. Labels directly underneath are sums of the 10-year variation in Wm^{-2} for the solar, water vapor, infrared and CO_2 absorption spectral regions, as also presented in Table 2, last column. Variation percentages (variation divided by average radiance) for each channel in ten years, shown in the bottom line, are marked in red for statistically significant channel changes above 1% of relative fluctuation.

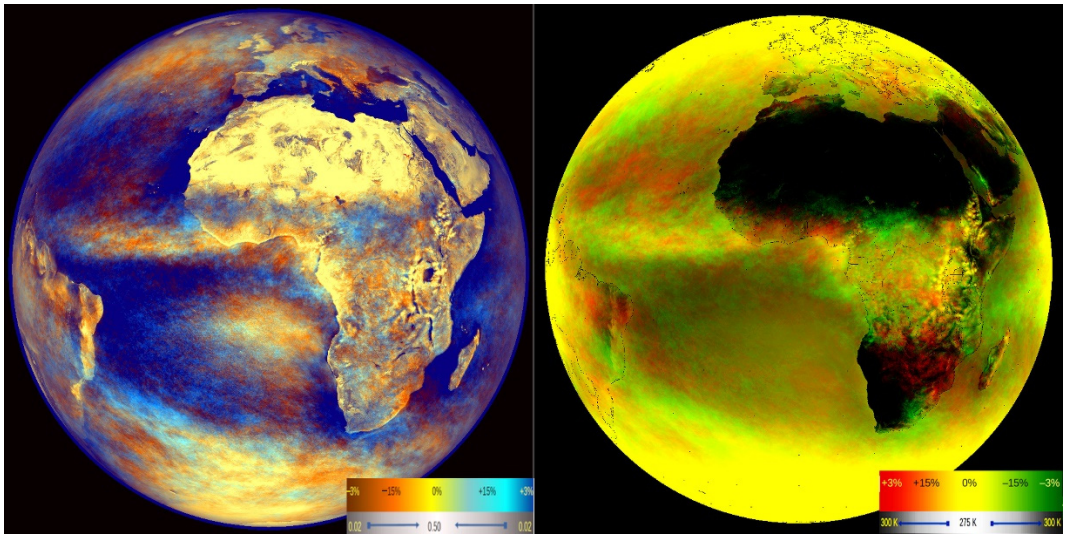

Figure 4. Decadal trend in percentage according to the color scale. (**Left**, for channel 0.6 µm), orange hues indicate a decrease in radiance to space and cyan hues an increase. Pixel color intensity indicates the average pixel reflectivity, from the error margin 0.02 (deep blue) to 0.50 (yellow). (**Right**, for channel 10.8 µm), orange hues mean an increase in the outgoing longwave radiation (OLR) and green hues a decrease, with average pixel intensity indicating brightness temperature, from 275 K, in yellow, to 300 K, in black.

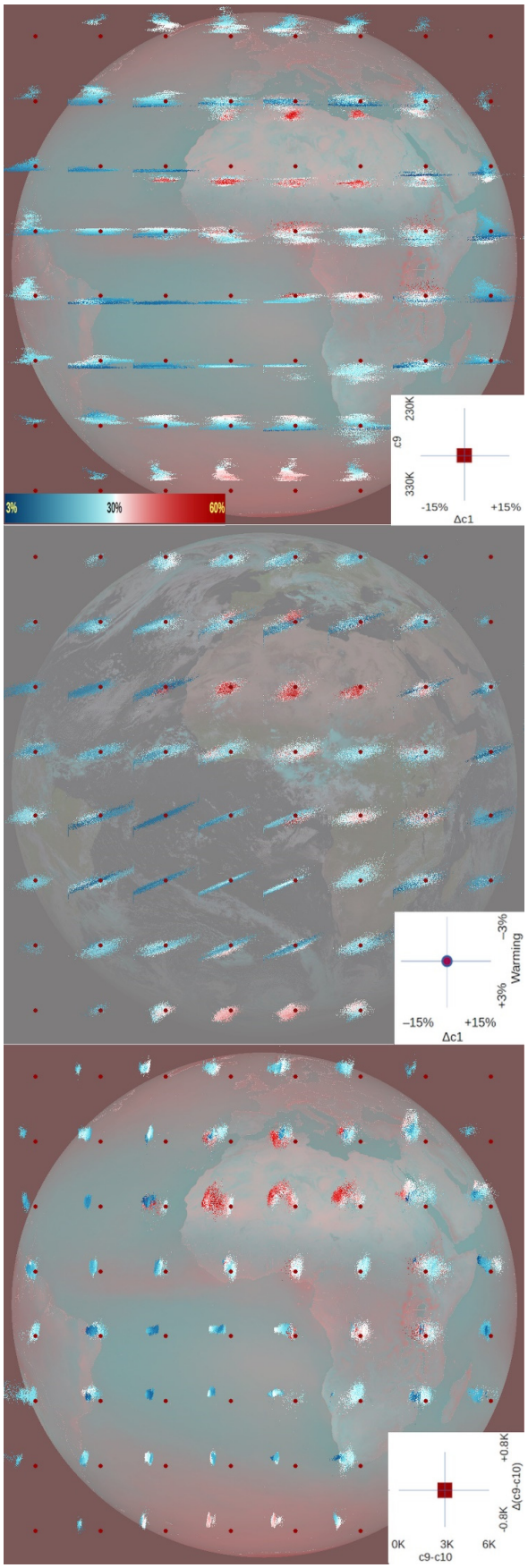

Figure 5. Geographic diagrams of the cloud change. Each scatter plot refers to the square satellite-projected region around the thick brown mark in its center. Dots (in shades blue to red) are read according

to the diagram in the lower right-hand corner of the three graphs in this figure. In all three images, pixels are represented by dots in a gradual reflectivity scale in the lower left-hand corner from 3% (blue dots, for locations with low solar reflectance) to 60% (red dots, high reflectance). (**Top**): for each of the 60 square regions in which we divided the MFoV, the graph relates average brightness temperature at 10.8 μm in ten years at 12 UTC (vertical axis) with decadal relative change in 0.6 μm reflectivity (horizontal axis); in other words, a heat- versus light-change. (See the inset in the lower right-hand corner for the precise limits.) For instance, for Mauritania, most pixels are very reflective and warm, and tend to lose 0.6 μm radiance in the 'recent' decade. (**Middle**): the regional graph dots again connect the pixel warming or cooling (vertical axis) with the relative variation in reflectivity at 0.6 μm (horizontal); e.g., a vertical value of +1% means a net decadal increase in the imbalance equivalent to 1% of the solar constant. (**Bottom**): correspondence of (vertical) change in the split-window brightness temperature difference (channel 10.8–12.0 μm) with (horizontal) difference value in the pixel (horizontal). Graph backgrounds are only provided for geographic reference.

For the interpretation of the atmospheric and ground evolution, we group Meteosat SEVIRI channels in four spectral categories (last column in Table 2 and Figure 3), which requires the integration of the measurements in solid angle. In the Lambertian hypothesis for radiative emission from a surface, channels get divided by a correction constant π to compensate for null values in the night. We encounter a limitation in how well the channels represent the spectral domain. As seen in the 4th column of Table 2, the bandwidths in SEVIRI channels partially overlap, and do not completely cover the infrared or solar domain. The channel grouping therefore introduces errors of $\pm 0.15\ \mathrm{Wm}^{-2}$ for each group of integrated radiances (last column in Table 2). That error estimate results from a Monte-Carlo approach on different choices of boundary values between the individual channels.

Table 2. Characteristics of Meteosat SEVIRI channels (labeled from 1 to 11) in columns 1 to 4. Estimates of average values of the spectral radiance (5th column) per channel. Wavenumber-integrated values (in Wm^{-2}) within the channel interval in the 6th column. Integrated radiance variation in 10 years (spectral values for the average difference of the observed pairs) in the 7th column. The 8th (last) column groups the integrated variations by spectral region, from the 7th column.

Domain	Meteosat Channel	Central Wavelength μm	Channel Boundaries μm	Spectral Radiance (in SPU) 10^{-3} Wm^{-2} sr^{-1} $(\mathrm{cm}^{-1})^{-1}$	Integrated Radiance Wm^{-2}	10-Year Change by Channel Wm^{-2}	Change by Domain Wm^{-2}
solar	1	0.64	0.56–0.71	3.91	22.7	−0.56	
solar	2	0.81	0.74–0.88	4.99	41.1	−0.42	sum solar = −1.07
solar	3	1.64	1.50–1.78	4.01	33.5	−0.10	(channels 1–4)
solar + infrared	4	3.92	3.48–4.36	0.83	3.2	0.01	
water vapor	5	6.25	5.35–7.15	3.29	10.6	0.14	sum WV = 0.11
water vapor	6	7.35	6.85–7.85	14.32	17.4	−0.03	(5–6)
infrared window	7	8.7	8.30–9.10	51.72	45.4	0.30	
infrared ozone	8	9.66	9.38–9.94	43.82	26.5	0.11	sum IR = 0.76
infrared window	9	10.8	9.80–11.80	86.80	47.3	0.25	(7–10)
infrared window	10	12.0	11.00–13.00	98.46	47.8	0.10	
CO_2 absorption	11	13.4	12.40–14.40	80.37	45.2	−0.58	CO_2 = −0.58 (11)

We integrate the spectral domain and angular domain to obtain radiances (in units Wm^{-2}) through the following formula:

$$\textit{Radiance variation} = \textit{Const} \times \textit{Spectral radiance variation} \times \textit{Channel spacing} \quad (1)$$

with *Const* = 1 for solar channels (numbers 1 to 4) and *Const* = π for infrared channels (from 5 to 11). The value (*Const* = 1) produces a 24 h average out of the measured day data at 12 UTC, assuming a typical cycle of 12 night hours and 12 h of day illuminations described by a positive sine function. *Channel spacing* is the width assigned to each channel in order to cover up the infrared spectral region while minimizing the inter-decadal channel variations.

The climate is driven by (a) the net amount of radiation entering and leaving the Earth atmosphere at its top, consisting of the Earth's reflected shortwave radiation (RSW) and the outgoing longwave radiation (OLR), plus (b) the heat absorbed or emitted by the deep oceans and, to a lesser extent, by the subsoil [17]. The former two quantities, RSW and OLR, can be respectively assessed from Meteosat solar channels (1 to 4) and infrared channels (5 to 11). The solar incoming radiation (SIR) varies with the Earth–Sun distance in the course of the year. (See [18] for details.)

As an equation for the climate imbalance (we call it CI here, but it is also often referred to as Earth Energy Imbalance, EEI) we use

$$CI = SIR - RSW - OLR \quad (2)$$

This imbalance is the difference between incoming and exiting radiation at the top of the atmosphere. It translates into the Earth surface-temperature change, with a growing trend in recent decades [19], plus the heat storage in the ocean and inner land layers. From the satellite perspective in Formula (2), any reduction in the satellite measured radiances (exiting the planet) means an increase in the imbalance, CI. We admit a limitation in the accuracy of the method beyond 14 μm, since no Meteosat channel covers that spectral region. We use a simple extrapolation for it, based on the values from SEVIRI channel 11 (Table 2). Given the problems around the strong Q branch for CO_2 absorption in the IASI OLR product [20], we dropped any external reference for the current imbalance at the ToA.

A summary of strengths and limitations in this study is presented in Table 3.

Table 3. Qualitative evaluation of the data and methods used in the study.

Aspect	Strength	Limitation
Source radiance data (SEVIRI)	High radiance accuracy after calibration and inter-calibration	Only for Meteosat field of view, not to be generalized to planet's surface
Spectral integration	More accuracy gained through averaging	Poor representation of SEVIRI channels in parts of the spectrum, e.g., above 15 μm
Radiation transfer simulation	Calibration based on CO_2 concentrations from other reliable sources	Disregards cross-absorption effects by several gases, and CO_2 impact beyond 14 μm. It can be corrected by comparison with IASI or AIRS.
Temporal data sampling	Large weekly independence, ENSO-Niño neutral on averages of two periods	Potentially exposed to multi-year anomalies in the large MFoV region. No consideration of night slots or conditions affecting emission
Connection to climate	Immediate connection of satellite radiances to climate variables, cloud and gas	Too short a period (20 years) for sound climate conclusions or sustained trends
Contribution to similar studies	Conclusions based on a wider spectral basis than in other studies (e.g., Loeb [11])	Discrepancies in the cloud evolution and fluctuation compared with other studies
Aerosol and cloud	Both atmosphere components are treated through a common reflectivity variable	Aerosol quantitatively disregarded in comparison with cloud changes
Future analyses	Easy translation to sub-regional trends in brightness temperatures	Geographical coverage limited to MFoV, requiring extra use of polar satellites (LEO) for a global analysis

3. Results

3.1. MFoV Global Trend Analysis

Figure 3 summarizes the spectrally integrated per-decade variation (in Wm^{-2}) for the eleven MSG channels, by comparing the 'recent' 10-year period (2015–2024, in blue) with the 'ancient' period 2005–2014.

We take the central wavenumbers of the MSG channels as the basis for the channel interval width estimation, and integrate in stereo angle and wavenumber. Excepting those at 7.3 μm and at 12 μm, the channels show statistically significant variations in the radiance per unit of wavenumber (usually expressed in cm^{-1}).

For the solar channels (SEVIRI channels 1 to 4) and for the CO_2 channel (SEVIRI channel at 13.4 μm) a negative radiance trend is observed. The radiances can be grouped in four regions by wavelength, as seen in Figure 3, and are labeled solar, water vapor, thermal infrared and CO_2 spectral domains. The radiance changes in Wm^{-2} for the four groups, with uncertainties of ± 0.15 Wm^{-2}, are also indicated. Most outstanding variations occur for channels centered at 0.6, 0.8, 6.2 and 13.4 μm. These results were already analyzed and commented on in [14], and they highlight the primary role of cloud in the flux balance at the ToA. The OLR around 0.2 Wm^{-2} for a decadal recent warming around 0.2 K is short compared with the hypothesis of linearity for the OLR on the surface temperature [21]: "The longwave clear-sky (LWCS) feedback has diverse spatial patterns in CMIP5 models, yet the global-mean feedback is robustly 1.9 $W/m^2/K$".

The outgoing radiance decrease in the CO_2 absorption region appears to be the consequence of the continuously increasing gas level, currently at a rate of about 6% per decade. The radiance decrease at channel 13.4 μm can be explained by that increase compounded with an increase in air temperature of (0.34 ± 0.08) K/decade. A similar air warming could also explain the measured increase at channel 5 around 6.2 μm. However, de-icing around the water vapor and CO_2 sensors in SEVIRI could also affect this channel accuracy. Water vapor channels have a limited impact, anyway, on the radiance balance, since they monitor a spectral region with low OLR. (See Figure 3 for a comparison with other regions.) The atmosphere specific humidity likely changed in ways we try to ascertain from channels at 10.8 μm and 12 μm [22], whose difference grows in every sub-region of the MFoV. (See Figure 5 (bottom image).)

The given values for air heating are confirmed by estimates from other data sources, which point to the recent record-low planetary albedo as the primary warming factor [23].

In fact, the Sahel Chad basin has lately received increased precipitation, similar to the precipitation during the high phase of the inter-decadal hydrological cycle in 1950–1960 [24,25]. This tallies in our study with the cyan hues in that region. We do not observe a clear pattern in the creation or destruction of cloud in the global MFoV, but an average reduction is clearly the trend.

Several studies [15,16] point out the prevalence of aerosol trends over greenhouse gas trends in climate warming: "Aerosol reductions significantly contribute to climate warming and increase the frequency and intensity of extreme weathers" [26]. We have not pursued this thesis here, because the weight of cloud in solar optical paths is 30–150 times stronger than the weight of aerosol [15], so it is easier to accept any recent reduction in cloud than a hundred times the same relative reduction in aerosol.

The relative variation for channel 10.8 μm (Figure 4, right) is not as high as for 0.6 μm, but firmly correlates with the solar decadal variation (Figure 4, left). A Pearson correlation coefficient of 0.71 is noted for the decadal variation in radiances at 0.6 μm and 10.8 μm, where a decrease in reflectance at 0.6 μm tends to match an increase in outgoing longwave radiation (OLR) at 10.8 μm. Even the 60 regions we distinguish in Figure 5 show, on average, that same pattern on the more local scale. Physically, a cloud reduction allows an

easier escape for heat from the ground. Above the Sahara, which is mostly cloud-free, there is no noticeable change in those two channels.

Figure 5 shows areas of geographical variation in the channel 0.6 μm reflectivity and combinations of radiance values in the infrared or their variation over the decade, namely 10.8 μm and 12.0 μm. A random selection of pixels in each regional square area is represented by colored dots, indicating their average reflectivity from 3% (in blue) to 60% (in red). We observe there the areas most affected by a decrease in RSW, namely the north Atlantic, eastern Europe, north-east Brazil and off the western coast of southern Africa. On the other hand, the Sahel, central Brazil and areas of the south Atlantic increased their cloud cover, as is also apparent above the warm Agulhas current [27].

3.2. Strong Regional Variability

Areas with less cloud in the final period than in the initial provide an easier escape route to space for the outgoing longwave radiation. The anomaly correlation for the regional changes in channels 0.6 μm and 10.8 μm is −0.46, and therefore significant, and also shows an intuitive result: with less cloud the Earth is able to release more heat into space, although reducing cloud leads to warming. Areas of increased outgoing longwave radiation (OLR) roughly correlate with areas of decreased reflected shortwave radiation (RSW), but with abundant exceptions. For example, the decrease in low-level cumulus cells hardly affects the OLR, since sea and low cloud have similar emission temperatures.

Desert regions like the Sahara, with scarce cloudiness and marginal land-cover transformation, show minimal changes in RSW but considerable variation in OLR over the 20 years. This can be explained by soil temperature increases, but this does not exclude aerosol (dust) changes. The Mediterranean area (Figure 5, top) shows a clear decrease in solar reflected radiation for those pixels with lowest reflectivity (sea pixels, blue dots), but little reduction for the land pixels (red dots). Maritime regions like the South Atlantic show high negative correlation between RSW and OLR. In such areas, with low presence of human-related aerosols, the registered change must be in the cloud amount. A decrease in the cloud cover optimally explains the fact that less solar radiation is reflected into space (negative RSW) and that more heat from the surface can reach space (positive OLR).

To identify high cloud, we counted pixels with particular thresholds in reflectivity and brightness temperatures as follows: reflectivity at 1.6 μm < 25% (as typical of ice cloud), at 0.8 μm > 90% (bright cloud), brightness temperature (BT) at 10.8 μm < 220 K (cold cloud) and difference BT 10.8 μm − BT 12 μm < 3 K (thick cloud). The number of pixels fulfilling all four conditions is not significantly different in the two decades considered. In this work, we disregard the night conditions. The cloud-cover decrease concerns mainly the low-level cloud. Warm cloud has a cooling effect on the planet, whereas high-level cloud is typically warming the surroundings, or occasionally having a neutral effect. We have not observed a variation in high-level cloud.

The decadal increase in brightness temperature around 10.8 μm (+0.32 K) and 12.0 μm (+0.20 K) is affected by changes in humidity, air temperature, or cloud cover. The difference between these two channels, which has increased by 0.12 K over the decade, is compatible with a (6 ± 2)% rise in specific humidity in the lower atmosphere or with an increase of (0.8 ± 0.2) K in low-level air temperature. A hypothetical decrease of about 6% in high-level cloud cover could also produce a similar differential warming of 0.12 K.

Our analysis of small regions, mainly depicted in Figure 5, shows a high variability among the 60 square regions distinguished within the MFoV in satellite projection, which can be interpreted individually. Red dots in the scattergrams indicate the most reflective pixels in the MFoV in the multi-year average. Blue dots stand for the darkest, and are usually linked to clear ocean surfaces.

1. The top image in Figure 5, with inset diagrams, shows the pixel connection between the infrared (IR) value of the pixel in kelvin (K) on the vertical axis, and its relative change in 0.6 μm radiation on the horizontal. That allows an identification of the temperature of the pixel most affected by the cloud reduction by just looking at the shift to the left-hand side in the dot distribution. For instance, in the north Atlantic west of the Iberian peninsula, it is the warmer pixels suffering dissipation (shift to the left). Off the coast of Namibia, there is a uniform reduction in low-level cloud, and typically dense fog in convective cells as a result of warm desert air sweeping above the cold Benguela current [28].
2. The middle image in Figure 5 shows pixel estimates by region for the warming, due to the decadal change in short- and long-wave radiation. Blue shades in the scatter plots reveal which cloud level is more influential in the regional warming or cooling. In most regions, it is the most reflecting pixels which are losing more reflectivity and contributing more to the positive climate imbalance (CI) at the top of the atmosphere. Note that a few values outside of the given boundaries for the horizontal are projected on the vertical axes.
3. The bottom image in Figure 5 shows regional changes for the difference in kelvin between channels at 10.8 μm and at 12.0 μm ('split-window difference'), which is globally a growth around 0.2 K in a decade. This increase might well be due to the higher specific humidity in the low levels of the troposphere, as a result of the increase in ocean and land temperatures. We did not find evidence of a general increase in high cloud or thin cirrus after exploring and counting pixels above particular thresholds defining that cloud. For instance, for the check on thick high cloud (HC), we used two periods of four years (2004–2008 and 2019–2023) and counted pixels fulfilling four criteria simultaneously (Figure 6):
   (a) Reflectivity at 1.6 μm < 25% (characteristic of ice-topped cloud)
   (b) Reflectivity at 0.8 μm > 90% (bright cloud)
   (c) Brightness temperature (BT) at 10.8 μm < 220 K (high thick cloud)
   (d) BT 10.8 μm − BT 12 μm < 3 K (thick cloud).

The resulting values of the fraction of pixels (around 6.0×10^{-4}) did not show a difference for the two periods, not even geographically (graph not shown). Pixels occur mainly in the equatorial region, around the Gulf of Guinea.

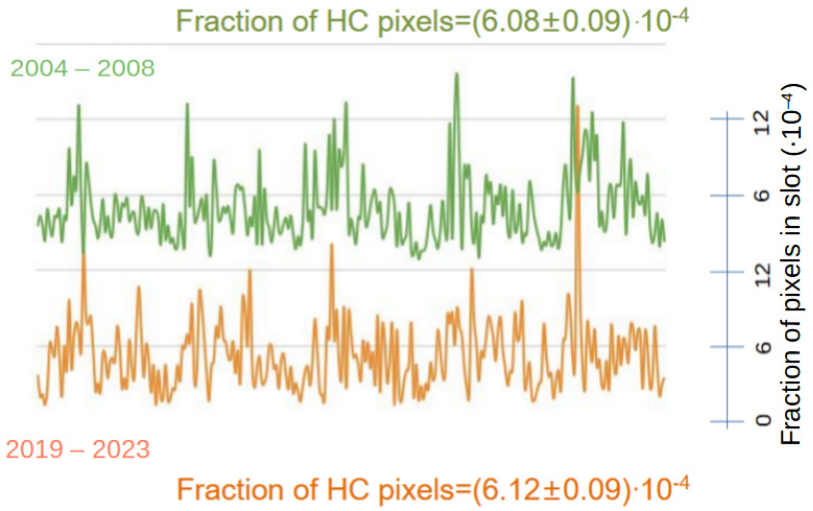

Figure 6. Pixel counts in two separate 4-year periods of Meteosat observations, showing no significant change in the fraction of thick high cloud (HC) over the MFoV for the evolution in two shorter periods (most remote and most recent in MSG records) of five years.

4. Over the Sahara, we notice a strong variation in the split-window difference, presumably not due to humidity changes, but perhaps to an increase in low-level air temperatures or vegetation in the Sahel region. An increase in greenness over large areas of the Sahel has been measured since the mid-1980s [29,30], in correspondence with an increase in cloud in our study (Figure 4, left).

3.3. Radiance Connection to Sea Surface Temperature (SST)

Using solely Meteosat radiances, we estimate sea surface temperature for every water pixel in the MFoV. Figure 7 provides the overall results for the average and decadal change in SST. The Mediterranean, Black Sea, around Madagascar, and the south Seas near Antarctica show the sharpest SST increases. North-west Atlantic and the Caribbean sea show SST cooling.

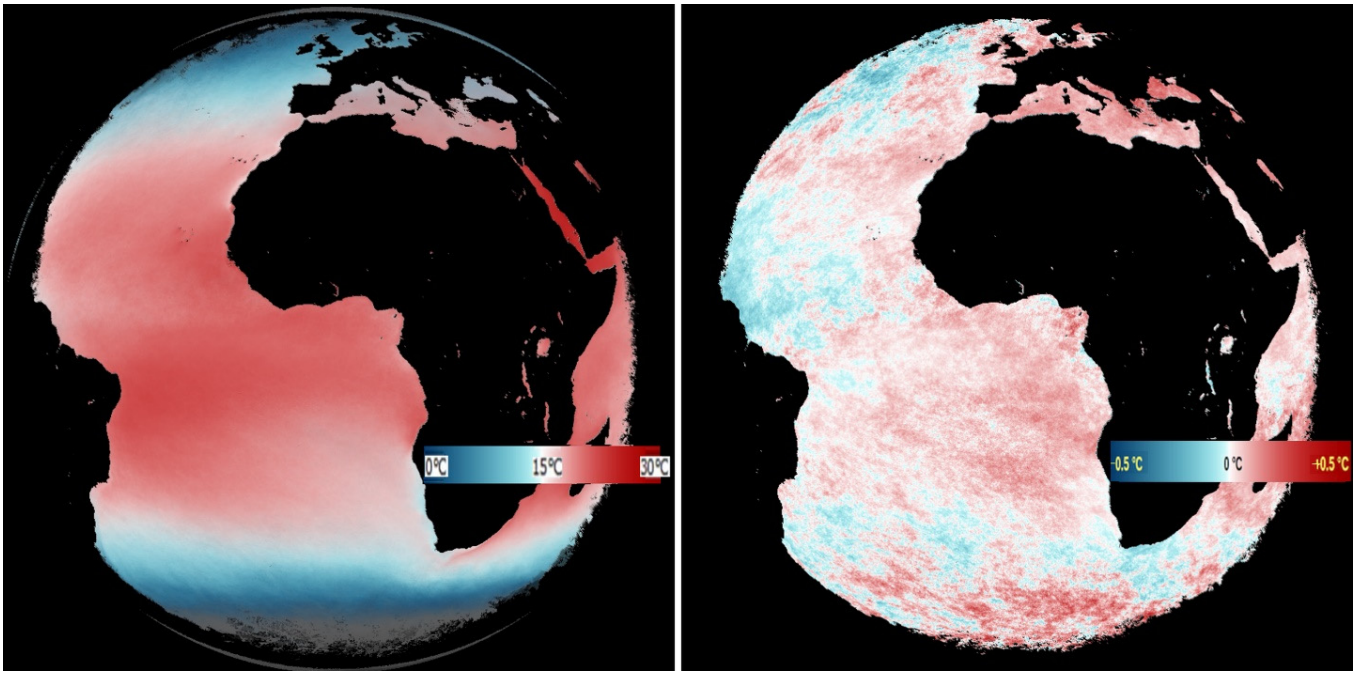

Figure 7. For sea or lake pixels, (**left**) shows the average value in the last decade of the sea surface temperature (SST) at 12 UTC. Equatorial regions show values approaching 30 °C, whereas mid-latitudes are closer to 15 °C for the annual average. (**Right**) shows the change in SST at 12 UTC in a decade, showing a variegated pattern of warmings and coolings, with a preponderance of the former. Polar pixels are frequently excluded from the estimate, due to almost permanent cloud.

3.4. SST Response to Climate Imbalance

Figure 8 should not be construed as showing absolute or confirmed values. In other words, the vertical axis can be shifted, in reality. Since imbalance is a weak indicator of the surface temperature rate, we have chosen the zero reference that best explains the accelerating heating in the last few years. The graph's worth lies in showing the imbalance in evolution over time, not the imbalance of actual values.

There is a strong connection between the climate imbalance (CI) and the SST change on the monthly time scale (Figure 8A). On the MFoV scale, SST warming occurs approximately between October and February, and cooling during the remaining months. What happens when we eliminate the seasonal variations with a 12-month filter of the imbalance and SST data? Then (Figure 8B) their correlation drops to +0.42, and we observe growth periods in one variable coinciding with level periods in the other. Both variables show a positive trend over the course of the 20 years. The lack of agreement is not surprising, given the complexities of the ocean internal dynamics, which we barely understand. Surface

measurements, and float studies on relatively few points, are vastly insufficient for a good comprehension [31].

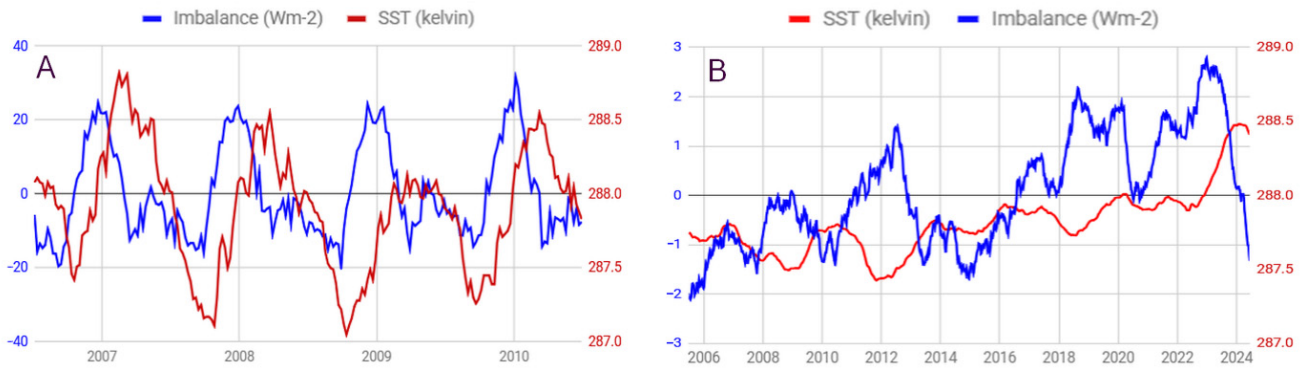

Figure 8. Left, letter (**A**): evolution of the climate imbalance (2006–2011) in blue, compared with the SST in the MFoV in red, showing the precise correspondence between the positive phases of the imbalance (from October to February) and the SST growth period, similar for all years. The imbalance leads by ten weeks the average-SST graph in the short term, with Pearson coefficient +0.71 between the two variables. Right, letter (**B**): on a longer time scale (2005–2024) with yearly running-averaged data, the two series display, however, a weak correlation (+0.42), pointing to ocean dynamics influence. Note: on the horizontal axes, the location of the year numeral marks the first week of that year.

We do not exclude some influence of El Niño cycles in the Atlantic SST variability. However, both decadal periods under consideration show a similar frequency for those anomalies [32].

The low cloud reduction, together with the increase in surface and atmosphere temperatures, explains the thermal infrared radiance increase. This result is very similar to the most recent data from CERES [33], which, however, shows a smaller change in the absorbed solar radiation. The reason is, perhaps, that CERES does not cover the last few hot years 2023–2025. Their OLR increase estimate matches ours.

Figure 9 offers a comparison of Meteosat SEVIRI and CERES short- and longwave measurements. This is a compelling proof of the lack of spurious trends in Meteosat, given the striking similarity of the series. The averaging of the CERES radiances was chosen with different weights, taking cosine (latitude) as a factor, both latitude and longitude, or no consideration for angles (as in our Meteosat slot averages). The differences in the CERES resulting series varied by less than 2%, and did not significantly affect the Pearson correlation coefficients.

The average imbalance during the sea surface warming seasons and the SST variation allows an estimate of the mixed-layer depth in ca. (35 ± 10) m, which is the layer of turbulence near the sea surface with homogeneous temperature and salinity. This depth is an average of north and south Atlantic conditions, and is close to typical values for tropical ocean waters.

Figure 10 shows the sea surface temperature evolution from January 2020 to June 2025 for different geographic subareas in the MFoV, illustrating a differential warming between the northern-hemisphere (NH) and the southern-hemisphere (SH) ocean portions. Other recent studies point to this same probable fact, which we have not yet studied in depth [34].

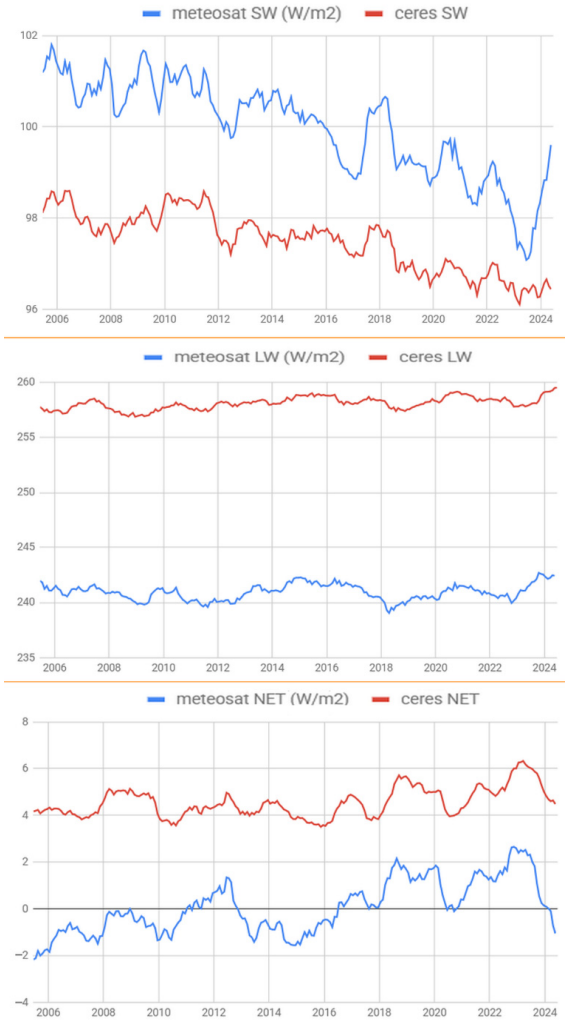

Figure 9. Comparison of measurements by CERES and SEVIRI (MSG) instruments, both in Wm^{-2}, on the two basic spectral bands, shortwave (solar, **upper** panel) and longwave (thermal infrared, **middle** panel), plus the net incoming radiance into the Earth system (**lower** panel). Pearson correlations between CERES and SEVIRI are strong, and around 0.74 ± 0.07.

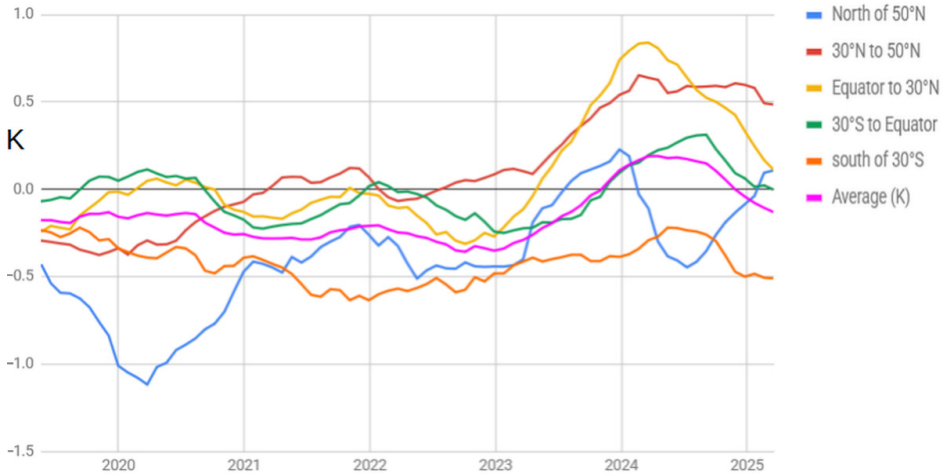

Figure 10. Deseasonalized evolution from July 2020 to February 2025 of the average SST anomaly (in kelvin on the vertical axis) for separate regions within the MFoV, and for the whole Atlantic as seen by Meteosat at 0 degrees ('Average'). The last 12 months' development in the curves shows warming in the high North latitudes and cooling of the tropical waters.

4. Discussion and Conclusions

This study analyzes two decades (2005–2024) of SEVIRI radiance measurements from the Meteosat Second Generation (MSG) satellites, to investigate interdecadal changes in top-of-atmosphere (TOA) radiation and cloud properties, and their relationship with sea surface temperature (SST) variability within the Meteosat field of view (MFoV). The results reveal coherent long-term changes in both the solar and thermal-infrared domains, with pronounced regional structure. The magnitude of these changes substantially exceeds that associated with variations in total solar irradiance over the same period [35], indicating that atmospheric and surface processes dominate the observed radiative evolution.

A persistent reduction in low-level cloud cover is identified across much of the MFoV, contributing to a decrease in reflected solar radiation and a positive TOA radiative imbalance. This finding is consistent with independent estimates from CERES observations and ERA5 reanalysis [21,33], and supports the role of low-level cloud variability as an important modulator of recent regional warming over both land and ocean surfaces.

The temporal evolution of the Meteosat-derived TOA imbalance closely resembles that inferred from CERES net incoming radiation for the same geographical domain, including comparable partitioning between solar and infrared components. Quantitatively, the decadal change in outgoing longwave radiation (-0.30 Wm^{-2} decade^{-1}) agrees well with previously reported values (-0.27 Wm^{-2} decade^{-1}), while somewhat larger differences are found in the absorbed solar component. The similarity between MFoV-based and near-global CERES estimates suggests that large-scale oceanic regions exhibit synchronized radiative variability on synoptic-to-interannual time scales.

Despite the clear radiative trends, the SST response exhibits distinct behavior on different time scales. On seasonal time scales, SST variations follow changes in the TOA radiative fluxes, whereas on interannual-to-decadal scales, SST evolution shows only weak correlation with the radiative imbalance (Pearson correlation before detrending of +0.35 to +0.41, depending on averaging type). No consistent time lag is identified that improves this coefficient. Over the last decade, Atlantic SSTs increased by ($+0.17 \pm 0.05$) K, while the corresponding decadal TOA imbalance amounts to ($+0.79 \pm 0.15$) Wm^{-2}, implying an effective heat-uptake depth of approximately 170 m, the zone reached by sunlight. This value is considerably deeper than the above estimate of 35 m for the mixed layer, suggesting that a substantial fraction of excess energy is redistributed below the immediate surface by other processes like diffusion, subduction, ocean currents, or eddies.

These results indicate that while TOA radiative imbalance governs short-term SST variability, long-term SST evolution is strongly influenced by heat exchange with deeper ocean layers. The observations support the view that SST alone provides an incomplete measure of ocean heat uptake, in agreement with previous studies estimating that the majority of excess energy is stored in the ocean interior [34]. The mechanisms controlling the partitioning of heat between surface and deeper layers remain incompletely characterized, and warrant further investigation.

Radiative imbalance estimates derived here are interpreted primarily in terms of their temporal evolution, rather than their absolute magnitude. Known uncertainties in spectrally resolved CO_2 absorption, particularly affecting some external OLR products, motivate this focus on relative changes. The robustness of the inferred trends is supported by their consistency across independent datasets and spectral domains.

The analysis further highlights a complex and regionally dependent relationship between cloud cover, SST, and TOA radiation. In several regions, similar reductions in cloudiness coincide with opposite SST tendencies, and no strong regional correlation between cloud changes and radiative imbalance is identified. These findings under-

score the importance of regional atmospheric and oceanic dynamics in shaping surface temperature responses.

Overall, this study provides observational evidence that low-level cloud variability has played a significant role in recent radiative changes over the Meteosat domain, while also demonstrating that ocean heat uptake and redistribution critically modulate the surface temperature response on decadal time scales. Long, stable geostationary satellite records such as those from Meteosat offer a valuable perspective on atmosphere–ocean coupling, and complement existing broadband and reanalysis-based assessments of climate variability.

Author Contributions: Conceptualization, J.I.P.-F.; methodology, J.I.P.-F.; software, J.I.P.-F.; validation, H.A.B. and J.I.P.-F.; formal analysis, J.I.P.-F. and H.A.B.; investigation, J.I.P.-F. and H.A.B.; resources, H.A.B. and J.I.P.-F.; data curation, J.I.P.-F.; writing—original draft preparation, J.I.P.-F. and H.A.B.; writing—review and editing, H.A.B. and J.I.P.-F.; visualization, J.I.P.-F. and H.A.B.; funding acquisition, H.A.B. All authors have read and agreed to the published version of the manuscript.

Funding: This study was partially supported by the Coordenação de Aperfeiçoamento de Pessoal de Nível Superior (CAPES 01/2022), Brazil, under the Project No. 88881.7050501/2022-01 to H.A.B through PEPEEC (Programa Emergencial de Prevenção e Enfretamento de Desastres Relacionados a Emergências Climáticas, Eventos Extremos e Acidentes Ambientais). It was also partially funded by budget funds from PraproSL, a commercial company based in Castuera, Spain.

Institutional Review Board Statement: Not applicable.

Informed Consent Statement: Not applicable.

Data Availability Statement: The data presented in this study are openly available in https://user.eumetsat.int.

Acknowledgments: This study uses as the main data source the Meteosat store from EUMETSAT, the European Organization for the Exploitation of Meteorological Satellites. Thanks are due to Richard Swifte for his selfless contribution to improve the text, and his valuable comments. Thanks also to Tim Hewison for his advice and expertise regarding the Meteosat calibration. The authors gratefully acknowledge the institutional support provided by the Laboratório de Análise e Processamento de Imagens de Satélites (LAPIS, at https://lapismet.com.br/), which facilitated data access.

Conflicts of Interest: The funders had no role in the design of the study, in the collection, analyses, or interpretation of data, in the writing of the manuscript, or in the decision to publish the results. Author J.I.P.-F. was employed by the company PraproSL. The remaining author declares that the research was conducted in the absence of any commercial or financial relationships that could be construed as a potential conflict of interest.

References

1. Dewitte, S.; Nevens, S. *Earth's Radiation Budget from 1979 to Present Derived from Satellite Observations*; Copernicus Climate Change Service (C3S) Climate Data Store (CDS): Bonn, Germany, 2021.
2. Xu, J.L.; Liang, S.L.; Jiang, B. A global long-term (1981–2019) daily land surface radiation budget product from AVHRR satellite data using a residual convolutional neural network. *Earth Syst. Sci. Data* **2022**, *14*, 2315–2341. [CrossRef]
3. Gupta, S.K.; Ritchey, N.A.; Wilber, A.C.; Whitlock, C.H.; Gibson, G.G.; Stackhouse, P.W. A Climatology of Surface Radiation Budget Derived from Satellite Data. *J. Clim.* **1999**, *12*, 2691–2710. [CrossRef]
4. Payez, A.; Dewitte, S.; Clerbaux, N. Dual View on Clear-Sky Top-of-Atmosphere Albedos from Meteosat Second Generation Satellites. *Remote Sens.* **2021**, *13*, 1655. [CrossRef]
5. Bojinski, S.; Verstraete, M.; Peterson, T.C.; Richter, C.; Simmons, A.; Zemp, M. The Concept of Essential Climate Variables in Support of Climate Research, Applications, and Policy. *Bull. Am. Meteorol. Soc.* **2014**, *95*, 1431–1443. [CrossRef]
6. Schmetz, J.; Pili, P.; Tjemkes, S.; Just, D.; Kerkmann, J.; Rota, S.; Ratier, A. An Introduction to Meteosat Second Generation (MSG). *Bull. Am. Meteorol. Soc.* **2002**, *83*, 977–992. [CrossRef]
7. Harries, J.E.; Russell, J.E.; Hanafin, J.A.; Brindley, H.; Futyan, J.; Rufus, J.; Kellock, S.; Matthews, G.; Wrigley, R.; Last, A.; et al. The Geostationary Earth Radiation Budget Project. *Bull. Am. Meteorol. Soc.* **2005**, *86*, 945–960. [CrossRef]

8. Harries, J.E.; Brindley, H.E.; Sagoo, P.J.; Bantges, R.J. Increases in greenhouse forcing inferred from the outgoing longwave radiation spectra of the Earth in 1970 and 1997. *Nature* **2001**, *410*, 355–357. [CrossRef] [PubMed]
9. Meirink, J.F.; Roebeling, R.A.; Stammes, P. Inter-calibration of polar imager solar channels using SEVIRI. *Atm. Meas. Tech.* **2013**, *6*, 2495–2508. [CrossRef]
10. Hewison, T.J.; Wu, X.; Yu, F.; Tahara, Y.; Hu, X.; Kim, D.; Koenig, M. GSICS Inter-Calibration of Infrared Channels of Geostationary Imagers Using Metop/IASI. *IEEE Trans. Geosci. Remote Sens.* **2013**, *51*, 1160–1170. [CrossRef]
11. Loeb, N.G.; Wielicki, B.A.; Doelling, D.R.; Smith, G.L.; Keyes, D.F.; Kato, S.; Manalo-Smith, N.; Wong, T. Toward Optimal Closure of the Earth's Top-of-Atmosphere Radiation Budget. *J. Clim.* **2009**, *22*, 748–766. [CrossRef]
12. Brindley, H.E.; Bantges, R.J. The Spectral Signature of Recent Climate Change. *Curr. Clim. Change Rep.* **2016**, *2*, 112–126. [CrossRef]
13. Samset, B.H.; Zhou, C.; Fuglestvedt, J.S.; Lund, M.T.; Marotzke, J.; Zelinka, M.D. Steady global surface warming from 1973 to 2022 but increased warming rate after 1990. *Commun. Earth Environ.* **2023**, *4*, 400. [CrossRef]
14. Fernández, J.I.P.; Georgiev, C.G. Evolution of Meteosat Solar and Infrared Spectra (2004–2022) and Related Atmospheric and Earth Surface Physical Properties. *Atmosphere* **2023**, *14*, 1354. [CrossRef]
15. Armour, K.C.; Collins, W.D.; Dufresne, J.-L.; Frame, D.J.; Lunt, D.J.; Mauritsen, T.; Palmer, M.D.; Watanabe, M.; Wild, M.; Zhang, H.; et al. *The Earth's Energy Budget, Climate Feedbacks, and Climate Sensitivity*; Forster, P.M., Storelvmo, T., Coords.; IPCC Sixth Assessment Report, Working Group I. World Meteorological Organization (WMO) & United Nations Environment Programme (UNEP); 2021. Available online: https://www.ipcc.ch/report/ar6/wg1/chapter/chapter-7/ (accessed on 25 June 2023).
16. Paulot, F.; Paynter, D.; Ginoux, P.; Naik, V.; Horowitz, L.W. Changes in the aerosol direct radiative forcing from 2001 to 2015: Observational constraints and regional mechanisms. *Atmos. Chem. Phys.* **2018**, *18*, 13265–13281. [CrossRef]
17. Copernicus Climate Change Service (C3S). Climate Indicators: Ocean Heat Content. 15 April 2025. Available online: https://climate.copernicus.eu/climate-indicators/ocean-heat-content (accessed on 18 October 2025).
18. Kidder, S.Q.; von der Haar, T.H. *Satellite Meteorology, an Introduction*; Academic Press: Cambridge, MA, USA, 1995; 466p.
19. Rohde, R. Global Temperature Report for 2024. Berkeley Earth, U.S. Non-Profit Organization Focused on Environmental Data Science and Analysis. Available online: https://berkeleyearth.org/global-temperature-report-for-2024/ (accessed on 14 March 2025).
20. Whitburn, S.; Clarisse, L.; Bauduin, S.; George, M.; Hurtmans, D.; Safieddine, S.; Coheur, P.-F.; Clerbaux, C. Spectrally Resolved Fluxes from IASI Data: Retrieval Algorithm for Clear-Sky Measurements. *J. Clim.* **2020**, *33*, 6971–6988. [CrossRef]
21. Zhang, Y.; Jeevanjee, N.; Fueglistaler, S. Linearity of Outgoing Longwave Radiation: From an Atmospheric Column to Global Climate Models. *Geophys. Res. Lett.* **2023**, *47*, e2020GL089235. [CrossRef]
22. Feng, J.; Paynter, D.; Wang, C.; Menzel, R. How atmospheric humidity drives the outgoing longwave radiation–surface temperature relationship and inter-model spread. *Environ. Res. Lett.* **2023**, *18*, 104033. [CrossRef]
23. Goessling, H.F.; Rackow, T.; Jung, T. Recent global temperature surge amplified by record-low planetary albedo. *Science* **2024**, *384*, 66–70. [CrossRef]
24. Salack, S.; Giannini, A.; Sarr, B. Rainfall trends in the African Sahel: Characteristics, processes, and causes. *Wiley Interdiscip. Rev. Clim. Change* **2016**, *7*, 367–388. [CrossRef]
25. Sylvestre, F.; Mahamat-Nour, A.; Naradoum, T.; Alcoba, M.; Gal, L.; Paris, A.; Cretaux, J.-F.; Pham-Duc, B.; Lescoulier, C.; Recouvreur, R.; et al. Strengthening of the hydrological cycle in the Lake Chad Basin under current climate change. *Sci. Rep.* **2024**, *14*, 24639. [CrossRef] [PubMed]
26. Wang, P.; Yang, Y.; Xue, D.; Ren, L.; Tang, J.; Leung, L.R.; Liao, H. Aerosols Overtake Greenhouse Gases Causing a Warmer Climate and More Weather Extremes Toward Carbon Neutrality. *Nat. Commun.* **2023**, *14*, 7257.
27. Stramma, L.; Cornillon, P.; Weller, R.A.; Price, J.F. Observations of Agulhas Current variability. *J. Geophys. Res. Ocean.* **1997**, *102*, 5513–5523. Available online: https://oceanrep.geomar.de/id/eprint/6196/ (accessed on 7 April 2026). [CrossRef]
28. Shannon, L.V.; Nelson, G. The Benguela: Large-Scale Features and Processes and System Variability. In *The South Atlantic: Present and Past Circulation*; Robinson, A.R., Brink, K.H., Eds.; Springer: Berlin/Heidelberg, Germany, 1996; Volume 11, pp. 163–210. Available online: https://www.sciencedirect.com/science/article/abs/pii/S0079661109001104 (accessed on 7 April 2026).
29. Olsson, L.; Eklundh, L.; Ardö, J. A recent greening of the Sahel—Trends, patterns and potential causes. *Atmosphere* **2005**, *63*, 556–566. [CrossRef]
30. Herrmann, S.M.; Anyamba, A.; Tucker, C.J. Recent trends in vegetation dynamics in the African Sahel and their relationship to climate. *Glob. Environ. Change* **2005**, *15*, 394–404. [CrossRef]
31. Roemmich, D.; Zilberman, N.V.; Thierry, V.; King, B.; Alford, M.; Andre, X.; Balem, K.; Van Wijk, E.M. Observing the full ocean volume using Deep Argo floats. *Front. Mar. Sci.* **2023**, *10*, 1287867. [CrossRef]
32. Ineson, S.; Scaife, A. The role of the stratosphere in the European climate response to El Niño. *Nat. Geosci.* **2009**, *2*, 32–36. [CrossRef]
33. Mauritsen, T.; Tsushima, Y.; Meyssignac, B.; Loeb, N.G.; Hakuba, M.; Pilewskie, P.; Cole, J.; Suzuki, K.; Ackerman, T.P.; Allan, R.P.; et al. Earth's energy imbalance more than doubled in recent decades. *AGU Adv.* **2025**, *6*, e2024AV001636. [CrossRef]

34. Cheng, L.; Abraham, J.; Hausfather, Z.; Trenberth, K.E. How fast are the oceans warming? *Science* **2019**, *363*, 128–129. [CrossRef]
35. Chatzistergos, T.; Krivova, N.A.; Yeo, K.L. Long-term changes in solar activity and irradiance. *J. Atmos. Sol.-Terr. Phys.* **2023**, *252*, 106150. [CrossRef]